Contemporary Mathematics
https://ojs.wiserpub.com/index.php/CM/

Research Article

Predicting Solar Cycles from ^{14}C and ^{10}Be Using Deep Neural Networks and Monte Carlo Simulations

Alouani Amira[1,2], Neila Bedioui[1,2], Mongi Besbes[1,2*]

[1] National School of Engineers of Tunis (RISC Lab LR16ES07), Laboratory of Robotics, Informatics and Complex Systems, University of Tunis EL Manar, Tunis, 1002, Tunisia
[2] Higher Institute of Information and Communication Technologies, University of Carthage, Borj Cedria, 1164, Tunis, Tunisia
E-mail: mongi.besbes@gmail.com

Received: 30 June 2025; **Revised:** 24 July 2025; **Accepted:** 28 July 2025

Abstract: The Sun is the primary source of energy for the Earth system, and fluctuations in solar activity exert a significant external influence on the planet's climate. Cyclical variations in solar irradiance can be inferred by studying changes in the concentrations of carbon-14 (^{14}C) and beryllium-10 (^{10}Be) isotopes. During periods of high solar activity (i.e., more sunspots), the enhanced solar wind and magnetic field shield the Earth from cosmic rays, reducing the production of ^{14}C and ^{10}Be in the atmosphere. In this study, various methods to predict future sunspot activity were explored, focusing on deep learning algorithms to develop predictive models. The learning process is based on historical records of ^{14}C, ^{10}Be, and sunspot data. The results obtained are both promising and encouraging, highlighting the potential for further advancements in this emerging area of research.

***Keywords*:** sunspots, solar cycles, ^{14}C, ^{10}Be, time series forecasting, deep learning, Long Short-Term Memory (LSTM), informer, Monte Carlo

MSC: 68P15, 68T07, 68W40, 86A08

Abbreviation

ADF test	Augmented Dickey-Fuller test
AI	Artificial Intelligence
AIC	Akaike Information Criterion
ARMA	Autoregressive Moving Average
BIC	Bayesian Information Criterion
Be10	Beryllium-10
C14	Radiocarbon (Carbon-14)
ESN	Echo State Network
HWES	Holt-Winters Exponential Smoothing
LSTM	Long Short-Term Memory
LightGBM	Light Gradient Boosting Machine
MA	Moving Average

DOI: https://doi.org/10.37256/cm.6420257651

MAE	Mean Absolute Error
MAPE	Mean Absolute Percentage Error
MASE	Mean Absolute Scaled Error
MV	Model Validation
NC	Normality Check
R^2	Coefficient of determination
RNN	Recurrent Neural Network
RMSE	Root Mean Squared Error
RSCN	Randomized Self-Constructing Neural Network
SC	Stationarity Check
SES	Simple Exponential Smoothing
TS	Time Series

1. Introduction

Solar activity [1] is a fundamental mechanism responsible for emitting radiation [2], energetic particles, and waves that impact not only the Earth but also other celestial bodies, the climate, and human existence. Understanding the fluctuations in sunspot activity over time represents a critical area of inquiry actively explored by numerous researchers [3]. Over the course of the last two centuries, a solar cycle has been characterized primarily by sunspot numbers [4], and this solar activity indicator has also been employed to forecast forthcoming solar activity [5].

For over a century, astronomers have observed that the number of sunspots, which are the dark patches appearing on the Sun's surface varies periodically, reaching a maximum every eleven years [6–8]. This is the solar activity cycle.

The study of solar activity poses a major scientific challenge due to its intrinsic complexity. Understanding solar cycles and accurately modeling them remains a daunting task. This complexity is further compounded by the lack of reliable measurements of solar spots, crucial elements in comprehending solar activity. The inherent variability of the sun, marked by periods of increased or decreased intensity, not only influences the spatial environment but also the planet itself. Efforts to forecast solar activity have been the focus of extensive research over many years, with significant contributions from researchers in this field. In recent times, this research has gained substantial momentum, leading to the publication of hundreds of journal articles dedicated to predicting the peak activity of solar cycles 24 and 25 [9]. A comprehensive analysis presented in [9, 10] of the recent predictions for these cycles indicates that while statistical and mathematical approaches yield widely varying results, physics-based predictions for the ongoing cycle 25 are converging and forecasting a relatively weak sunspot cycle. This forecast aligns with observations of the developing solar cycle.

In addition to direct observations, proxy data from cosmogenic isotopes such as beryllium-10 (^{10}Be) and carbon-14 (^{14}C) have proven valuable in reconstructing past solar activity and improving prediction models. These isotopes are produced in the Earth's atmosphere through interactions with cosmic rays, which are modulated by solar magnetic activity. During periods of high solar activity, the intensified solar wind and magnetic field shield the Earth from cosmic rays, resulting in reduced production of ^{10}Be and ^{14}C. Conversely, higher isotope concentrations correspond to solar minima. Because these isotopic records are preserved in natural archives such as ice cores and tree rings, they offer a long-term perspective on solar variability, making them essential tools for understanding and forecasting sunspot cycles in the absence of consistent instrumental data.

Time series analysis plays a pivotal role in the prediction of sunspots, providing valuable insights into the cyclical and ever-changing nature of solar activity. Sunspot data, collected over centuries, form a chronological record of observations, rendering them exceptionally suitable for time series analysis. By examining historical sunspot patterns and their temporal characteristics, scientists can discern recurring cycles, notably the well-documented approximately 11-year solar cycle. Employing various time series techniques, including advanced deep learning methods, researchers can create models and forecasts for forthcoming sunspot activity by extrapolating from historical trends and periodic behaviors. These forecasts not only enhance the comprehension of short-term sunspot fluctuations but also make significant contributions to the broader domain of space weather forecasting. This knowledge about solar activity is essential for a multitude of

applications, encompassing satellite operations, radio communications, and the management of potential solar-induced disturbances on Earth. Therefore, time series analysis offers a robust framework for leveraging historical sunspot data to make well-informed predictions about future solar activity.

To achieve this, two advanced deep learning architectures were employed: the Long Short-Term Memory (LSTM) network and the Informer model. The LSTM is particularly effective for capturing temporal dependencies in sequential data, while the Informer is designed to handle long time series with high efficiency and accuracy. The performance of these models is compared to evaluate their effectiveness in modeling and forecasting sunspot activity based on proxy isotope data.

A key innovation in this approach is the application of the Monte Carlo method to reduce the variance of the predictions. By applying this statistical technique, multiple simulated outcomes are generated and subsequently averaged to derive a more robust estimate. This process not only enhances the accuracy of the sunspot number estimations but also reduces the uncertainty associated with them.

The combination of these advanced methodologies represents a significant step forward in the field of solar activity estimation. The approach not only offers a higher degree of precision but also provides a framework that can be adapted to other areas of climate and environmental research where accurate long-term predictions are essential. This study demonstrates the potential of combining paleoclimatic data with cutting-edge machine learning techniques, paving the way for more sophisticated models in future research.

The rest of this work is organized and structured as follows:

Section 2 describes a brief outline of the methodology and key findings with an overview of the analytical approaches employed, including statistical tests and time series prediction models. The focus is placed on time series, assessing their relevance within the context of forecasting, describes data collection and exploratory data analysis. This section delves into the formulation of the model and the methods used for evaluation. Section 3 presents and analyses the results obtained from deep learning algorithms. Comparison of model performance and insights gained from the analysis of isotopic records and sunspot observations. Discussions of the implications of the findings for understanding solar dynamics and predicting future solar activity are given in this section. Section 4 conclusions are made.

2. Methodology

To overcome these challenges, different approaches describing multivariate methods are presented in this study. By integrating multiple data processing algorithms, the methodology aims to minimize biases and enhance measurement reliability. The methodology flowchart presented in Figures 1, 2 and 3 illustrates this work, highlighting the sequence of steps required to merge data from different sources and apply correction and optimization techniques. By adopting a holistic and integrated approach, the methodology aims to provide a more precise and comprehensive understanding of solar activity, thus opening new avenues for research in solar astronomy and its implications for the understanding of climate and the surrounding space.

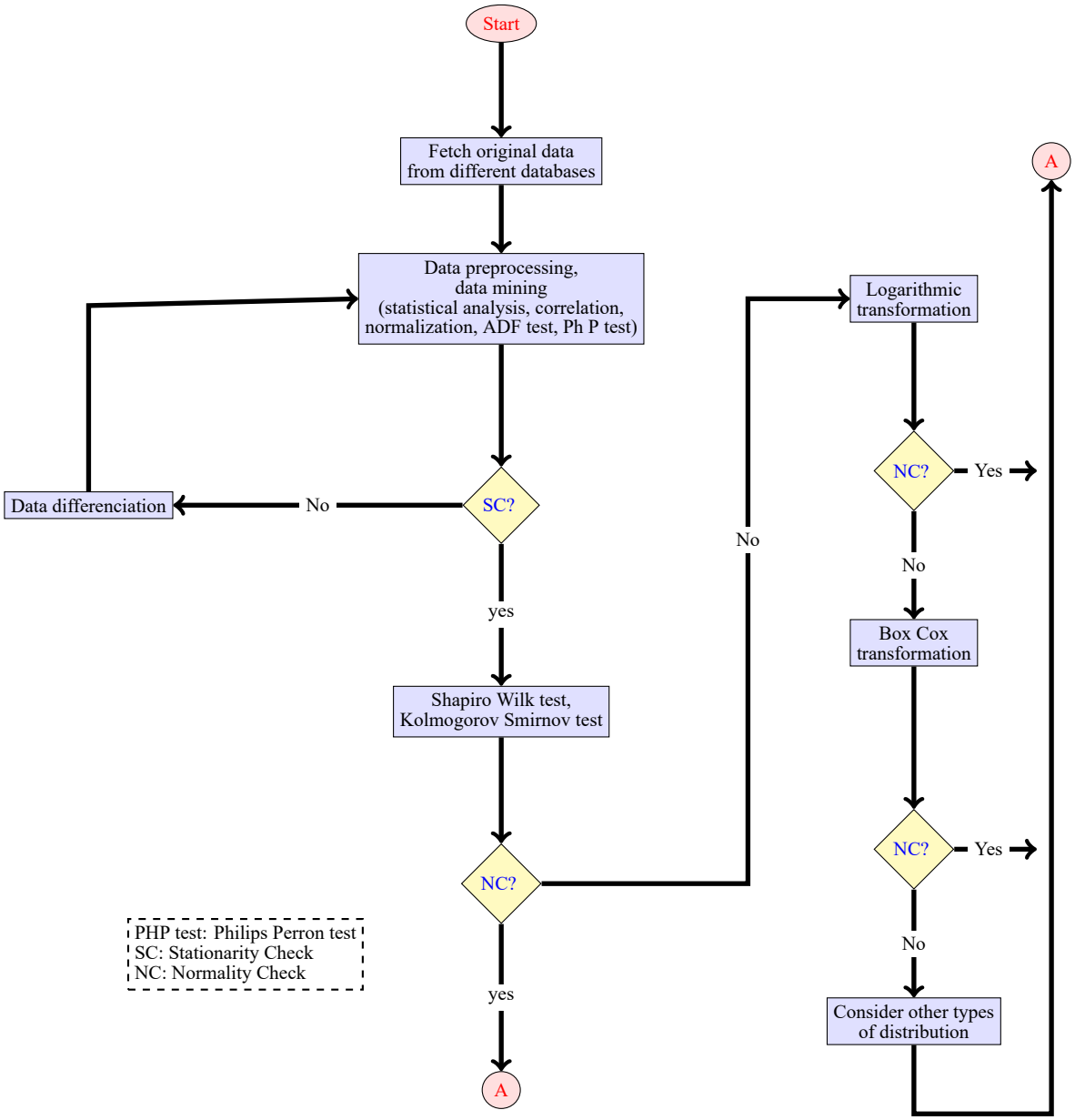

Figure 1. The proposed methodology flowchart utilized to predict sunspot number: Data preprocessing and statistical preparation

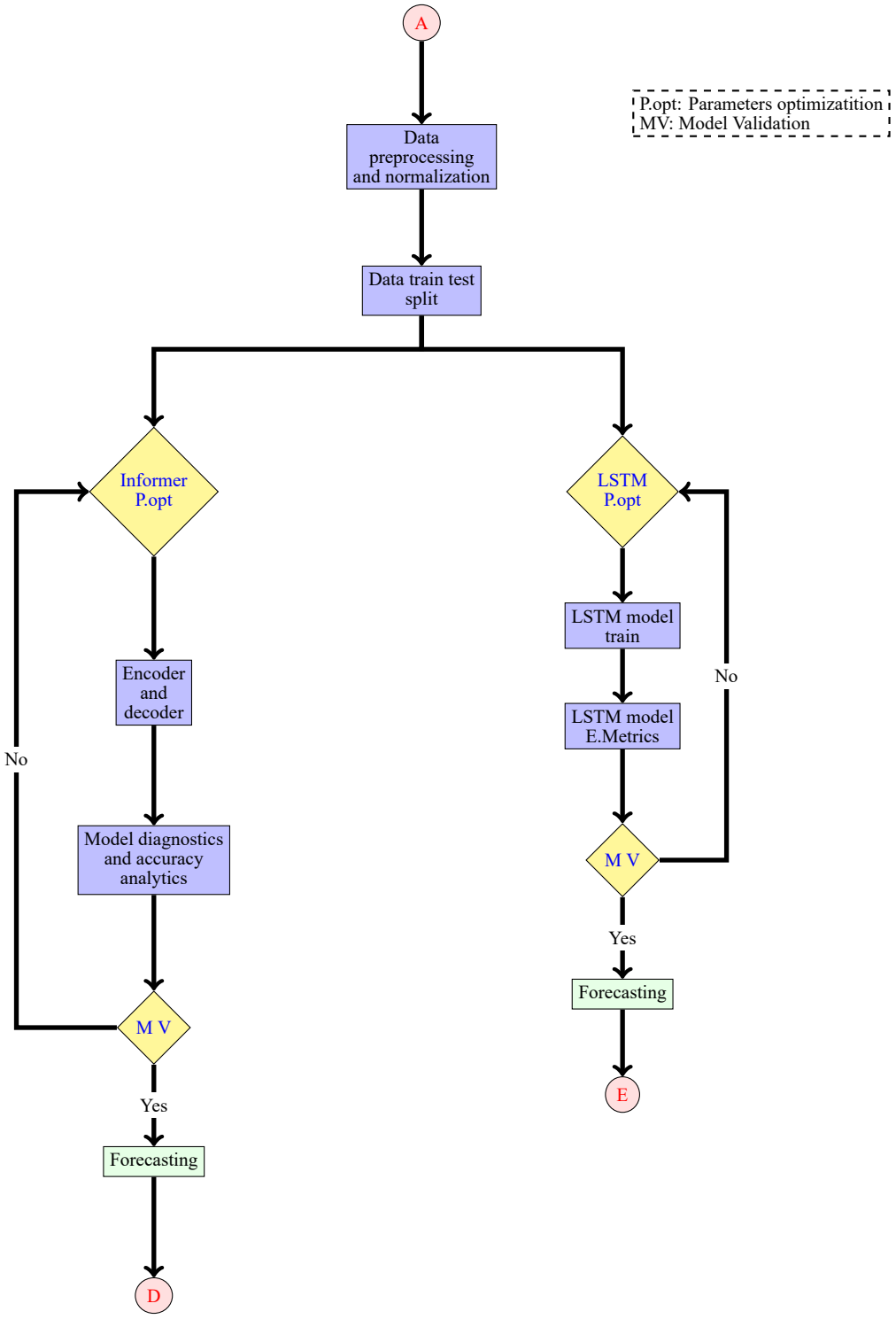

Figure 2. The proposed methodology flowchart utilized to predict sunspot number: Multivariate forecasting with LSTM and Informer models

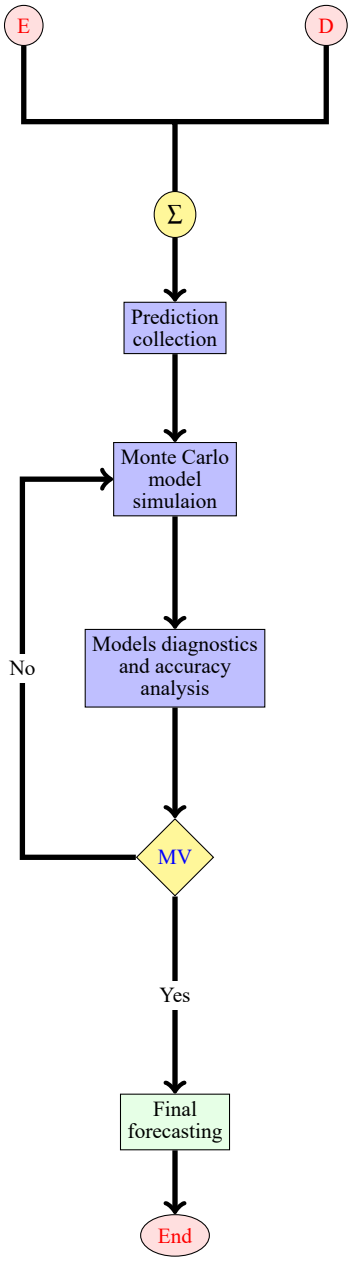

Figure 3. The proposed methodology flowchart utilized to predict sunspot number: Aggregation, Monte Carlo simulation, and final forecast

2.1 *Data collection*

A comparative study will be conducted on a database representing measurements of solar sunspots, based on real curves published in the literature [11, 12]. In order to build the dataset it's important to highlight that the measurement of solar sunspots can be predicted based on measurements of the carbon isotope ^{14}C and beryllium isotope ^{10}Be.

The dataset consist of observations spanning from 982 to 1927. The data includes four columns: the year, sunspot activity, ^{10}Be concentration, and ^{14}C concentration. These variables are recorded at regular time intervals and will be used to study relationships between solar activity, ^{10}Be, and ^{14}C measurements over time.

A recent method for predicting sunspots, which has garnered significant attention, leverages isotopes as a novel predictor. This approach is grounded in the study of isotopic variations within terrestrial archives, such as ice cores and

tree rings, which can capture the historical intensity of cosmic rays hitting the Earth. Since the solar magnetic field, which undergoes variations over the solar cycle, modulates the flux of cosmic rays reaching Earth, isotopes like ^{10}Be and ^{14}C can serve as indirect proxies for solar activity, including sunspots. Scientists analyze these isotopic data to reconstruct past solar cycles and predict future solar activity by identifying patterns and correlations between isotopic concentrations and sunspot numbers. This method provides a unique and valuable perspective by extending the ability to study solar activity beyond the period of direct observations, offering insights into the long-term behavior of the Sun.

Cosmogenic radionuclides [13] are continually formed within the Earth's atmosphere as a result of the impact of highly energetic particles called cosmic rays. The rate of their generation in the atmosphere is influenced by various factors, including the intensity of galactic cosmic rays, the solar activity levels, and the Earth's geomagnetic field's strength. Solar activity can be quantified by utilizing the solar modulation parameter ϕ (measured in MeV), which describes the Sun's magnetic field's effectiveness in shielding against galactic cosmic rays. This parameter can be determined based on the worldwide production of cosmogenic nuclides. Numerous radioisotopes originate from cosmic ray and secondary neutron interactions with atmospheric atoms. In this process, atoms can either undergo neutron capture or engage in spallation reactions, resulting in their conversion into radioactive elements.

Beryllium 10 is created when atmospheric oxygen and nitrogen nuclei burst under the impact of a cosmic ray particle. Once formed, ^{10}Be atoms attach themselves to aerosols and are transported by atmospheric circulation. It is estimated that they are transported for around a year and a half, before being deposited by rain or snow in polar ice caps or in marine and lake sediments, from which they can be extracted for measurement.

During periods of high solar activity, such as when there are many sunspots present, the Sun's magnetic field is stronger, deflecting more cosmic rays away from the Earth. This results in a decrease in the production of ^{10}Be in the atmosphere. Conversely, during periods of low solar activity, when sunspot activity is minimal, the Sun's magnetic field weakens, allowing more cosmic rays to penetrate the Earth's atmosphere and leading to increased production of ^{10}Be. Scientists can analyze concentrations of ^{10}Be in ice cores, tree rings, and sediment layers to reconstruct past solar activity levels. By studying the variations in ^{10}Be concentrations over time, researchers can infer patterns of solar activity, including the occurrence of solar minimums and maximums, and the frequency and intensity of sunspot cycles.

Carbon-14, which results from the capture of a neutron (with the emission of a proton) by a Nitrogen-14 atom. ^{14}C is a radioactive isotope of carbon, with a half-life of approximately 5,730 years. It is formed continuously in the Earth's atmosphere through the interaction of cosmic rays with nitrogen atoms. This radioactive carbon is then absorbed by living organisms through processes such as photosynthesis or consumption of food. As a result, ^{14}C becomes incorporated into the tissues of plants and animals at a constant rate.

The relationship between carbon-14 and sunspots is intertwined through the phenomenon of solar activity. Solar activity, including the number and intensity of sunspots, affects the Earth's atmosphere in several ways. One significant impact is on the production of ^{14}C.

2.2 *Data preprocessing*

In the realm of solar research, especially when examining sunspot activity through the lens of ^{14}C and ^{10}Be isotopic data, the deployment of time series analysis tools is pivotal. These tools encompass a variety of statistical and computational techniques designed to analyze temporal data, identify patterns, and forecast future values based on historical trends.

Stationarity refers to the property of a random process where its statistics, such as mean, autocorrelation, and distribution, remain unchanged over time. A time series is considered stationary when its observations are independent of time, meaning that its statistical characteristics remain constant, including mean, variance, and covariance. On the other hand, Time serie containing trends or seasonality are non-stationary. Trends introduce a systematic change in the data over time, altering the mean, while seasonality causes variations in a regular time interval, leading to changes in variance. In order to make accurate forecasts and predictions, it is important for the time series data to exhibit stationarity. Various methods exist to validate the stationarity assumption and transform time series data into a stationary form.

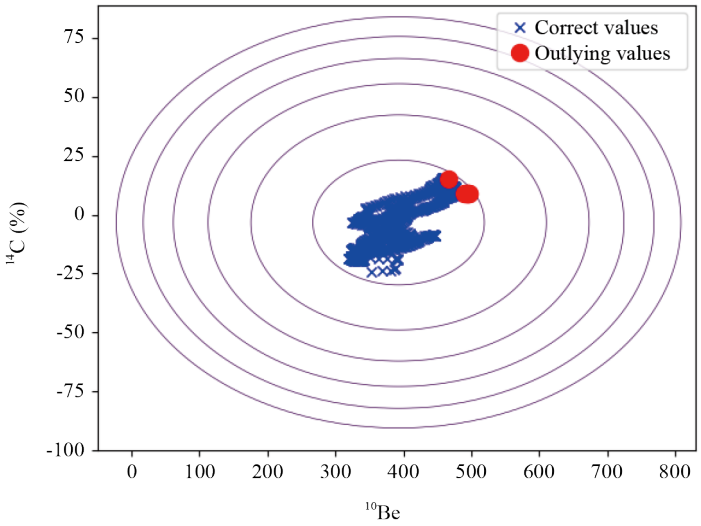

Figure 4. Anomalies detection

The Figure 4 illustrate the detection of some outliers in the ^{14}C and ^{10}Be measurements dataset. This can be explained by measurement anomalies due to the diversification of data collection methods for these measurements.

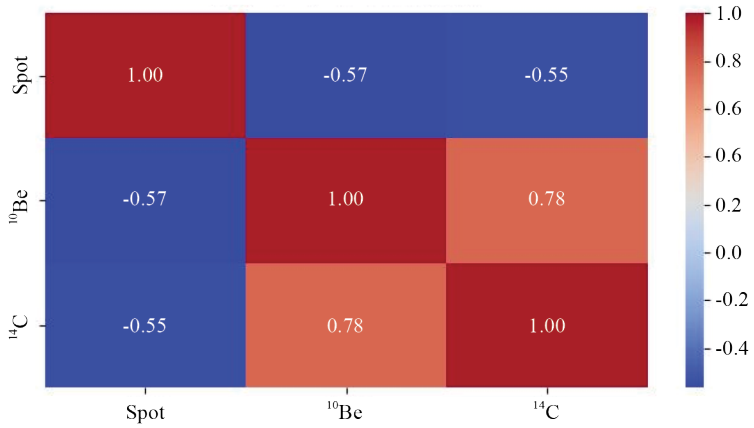

Figure 5. Feature correlation matrix

This correlation matrix in Figure 5 represents the correlations between three features: sunspot, ^{10}Be and ^{14}C. The value of 1 along the diagonal indicates that each feature is perfectly correlated with itself, as expected. The correlation coefficient between spot and ^{10}Be is -0.57, indicating a moderate negative correlation between these two features. This suggests that as the value of one feature (spot) increases, the value of the other feature ^{10}Be tends to decrease, and vice versa, although the relationship is not strong.

Similarly, the correlation coefficient between spot and ^{14}C is -0.55, also indicating a moderate negative correlation between these two features. This suggests an inverse relationship where an increase in one feature is associated with a decrease in the other feature, and vice versa, although the correlation is not strong.

Lastly, the correlation coefficient between ^{10}Be and ^{14}C is 0.78, indicating a strong positive correlation between these two features. This suggests that as the value of one feature ^{10}Be increases, the value of the other feature ^{14}C tends to increase as well, and vice versa.

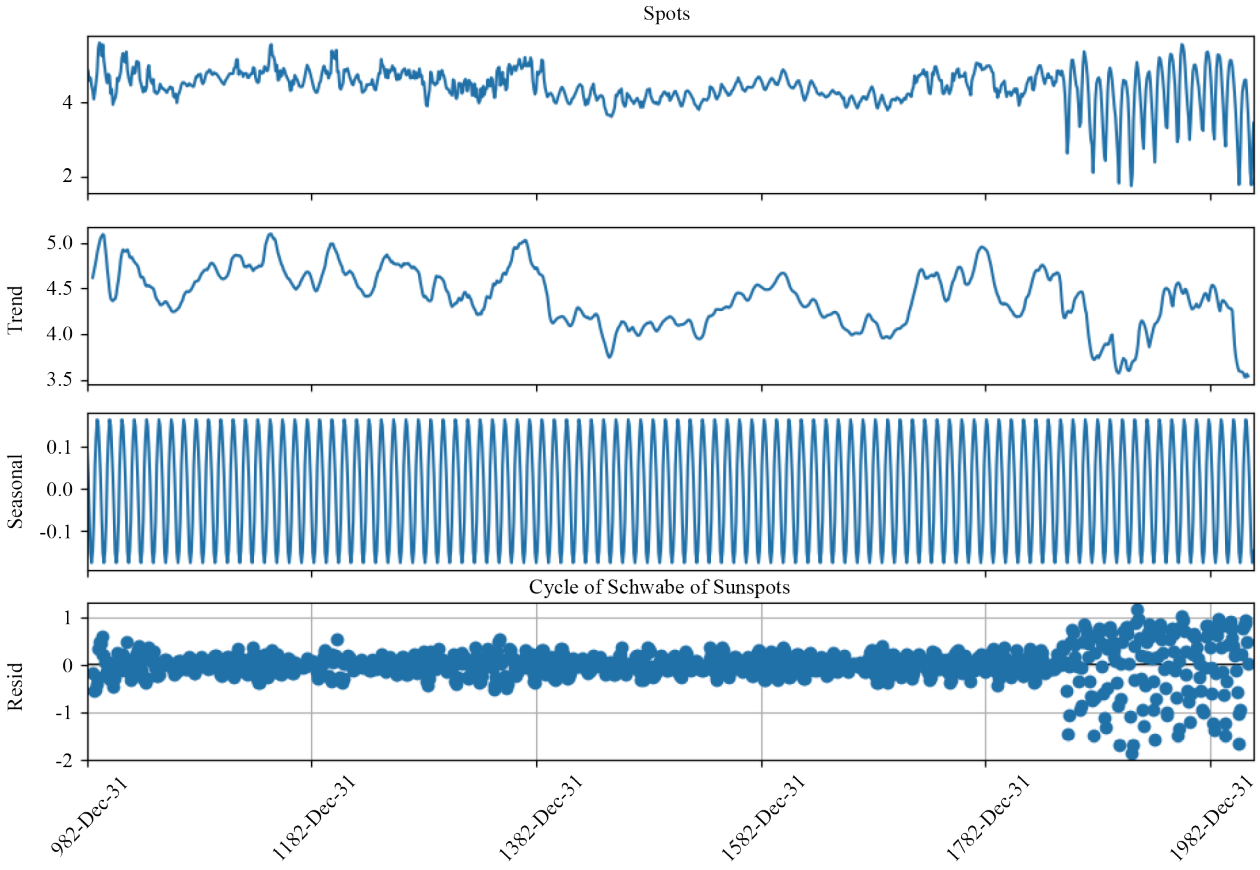

Figure 6. Schwabe cycle

The best-known solar activity cycle, Schwabe cycle, averaging eleven years, is identified by counting sunspots, the number of which is directly related to the Sun's irradiance (or solar constant). From counting archives, a quasi-continuous serie, ranging from annual to daily, has been reconstructed. This serie, representing the number of sunspots, exhibits a very pronounced 11-year cyclicality, with cycle durations ranging from 9 to 13 years as showen in Figure 6.

Autocorrelation, also known as serial correlation, measures the correlation of a time series with a lagged version of itself. It is a fundamental concept in time series analysis used to detect patterns or dependencies between observations at different time lags.

The autocorrelation coefficient at lag k, denoted by r_k, is given by the following equation:

$$r_k = \frac{\sum_{t=k+1}^{n} (y_t - \bar{y})(y_{t-k} - \bar{y})}{\sum_{t=1}^{n} (y_t - \bar{y})^2} \tag{1}$$

Where y_t is the value of the time series at time t, $\bar{y}$ is the mean of the time series, k is the lag (i.e., the number of previous time steps considered) and n is the total number of observations in the series. The numerator of the autocorrelation formula represents the covariance between the time series and its lagged version, while the denominator serves to normalize this value using the total variance of the series. The resulting autocorrelation coefficient r_k takes values between -1 and 1. A value close to 1 indicates strong positive autocorrelation at lag k, meaning past values are positively associated with future

values at that lag. Conversely, a value close to −1 indicates strong negative autocorrelation. A value near 0 implies little to no autocorrelation, suggesting that values at lag k are not significantly related to each other.

In the figure of autocorrelation histograms for sunspots, shown in Figure 7, observing bars increasing towards 1 and then decreasing towards 0 in a periodic manner signifies a cyclic or seasonal autocorrelation pattern within the sunspot data. This periodic behavior indicates a significant correlation between sunspot observations at specific time lags, followed by a decline in correlation as the lag increases or decreases.

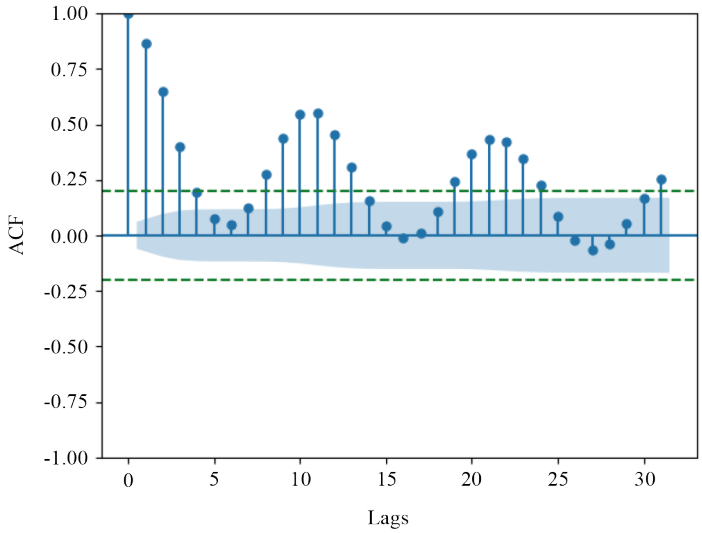

Figure 7. Autocorrelation for sunspots

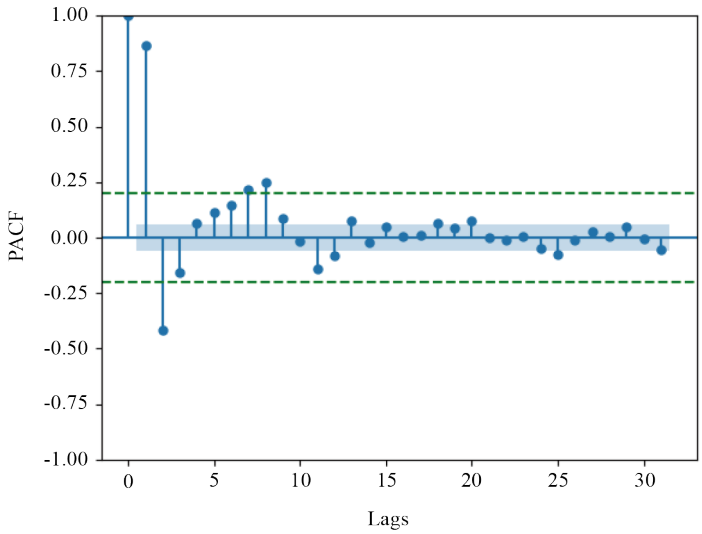

Figure 8. Partial autocorrelation for sunspots

Sunspot activity exhibits cyclic patterns, known as the solar cycle, typically spanning approximately 11 years. During this cycle, sunspot numbers increase, reaching a maximum (solar maximum), and then decrease to a minimum (solar minimum) before beginning a new cycle (Schwabe cycle). The autocorrelation histogram reflecting this cyclic behavior

suggests that sunspot activity at a particular time is significantly correlated with sunspot activity at a certain lagged time, corresponding to the periodicity of the solar cycle.

In the context of a partial autocorrelation histogram for sunspots in Figure 8, where bars are close to 0, this suggests a lack of significant partial autocorrelation beyond the immediate lag. Each observation of sunspot activity appears to be largely uncorrelated with its previous observations once the influence of the immediate lag (lag 1) is accounted for.

This finding indicates that while there may be some short-term dependence between consecutive observations, the correlation diminishes rapidly beyond the immediate lag. The absence of significant partial autocorrelation suggests that the sunspot activity at any given time is largely independent of its historical values beyond the immediate past. Understanding this lack of long-term autocorrelation in sunspot data is important for modeling and predicting future sunspot activity. It implies that past sunspot activity may not be a strong predictor of future activity beyond the short term. Instead, other factors such as solar physics, magnetic fields, and external influences may play more significant roles in determining future sunspot behavior.

2.2.1 *ADF test*

The Augmented Dickey-Fuller test, commonly referred to as the *ADF test*, is widely used to assess the stationarity of a Time Series (TS). This method is essential because most forecasting models assume that the underlying time series is stationary. The ADF test belongs to a broader class of statistical tests known as unit root tests. The core idea behind these tests is to evaluate the extent to which a time series is influenced by a deterministic trend. The ADF test employs an autoregressive model and determines the optimal number of lags using information criteria such as AIC or BIC, thereby accounting for higher-order correlation structures in the data.

The null hypothesis of the ADF test asserts that the time series has a unit root, indicating non-stationarity and the presence of a time-dependent structure. Conversely, the alternative hypothesis implies stationarity, meaning that statistical properties such as the mean and variance remain constant over time.

$$\Delta y_t = \alpha + \beta t + \gamma y_{t-1} + \sum_{i=1}^{p} \delta_i \Delta y_{t-i} + \varepsilon_t \tag{2}$$

Where: y_t represents the time series being tested, and $\Delta y_t = y_t - y_{t-1}$ is the first difference of the series. The term α denotes the constant or drift component, while βt represents the deterministic time trend. The parameter γ is the coefficient of interest; if $\gamma = 0$, it indicates the presence of a unit root, suggesting that the time series is non-stationary. The coefficients δ_i correspond to the lagged differences Δy_{t-i}, which help account for higher-order autocorrelation. The number of lagged terms included is denoted by p, chosen to ensure white noise residuals. Finally, ε_t is the white noise error term.

Table 1. ADF test results

Tests	ADF statistics	p-value	1%	5%	10%
Spots	-3.672	0.004	-3.436	-2.864	-2.568
Beryllium 10	-2.205	0.204	-3.436	-2.864	-2.568
Carbon 14	-1.204	0.671	-3.436	-2.864	-2.568

The Table 1 presents the results of the Augmented Dickey-Fuller (ADF) test conducted on three different datasets: Spots, ^{10}Be, and ^{14}C. The ADF statistic for Spots indicates that there is strong evidence to reject the null hypothesis of a unit root and suggests that the Spots dataset is likely stationary. This inference is further supported by the low p-value (0.004), which is below the conventional significance level of 0.05, indicating a high level of confidence in the result. Conversely,

for the ^{10}Be and ^{14}C datasets, the ADF statistics are smaller in magnitude and accompanied by higher p-values (0.204 and 0.671, respectively). These results suggest that there is insufficient evidence to reject the null hypothesis of a unit root, indicating that the ^{10}Be and ^{14}C datasets are likely non-stationary. Measurements of ^{14}C and ^{10}Be are non stationary because these isotopes undergo radioactive decay processes and are also subject to complex environmental interactions such as transportation by rivers, absorption by living organisms, and sequestration in geological formations, resulting in their variation over time.

2.2.2 *Shapiro-Wilk test*

The Shapiro-Wilk test is a statistical method used to assess whether a data sample follows a normal distribution. It is extensively applied in statistical analysis to verify the assumption of normality, which underlies many parametric tests. The Shapiro-Wilk test utilizes test statistics based on regression coefficients to determine if the data significantly deviate from a normal distribution. Specifically, it evaluates how closely the ordered sample values match those expected from a normal distribution.

The null hypothesis H_0 of the Shapiro-Wilk test states that the data sample is drawn from a normal distribution, while the alternative hypothesis H_a posits that the data sample does not follow a normal distribution. If the p-value resulting from the test is less than a chosen significance level (e.g., 0.05), the null hypothesis is rejected, indicating non-normality. If the p-value is greater than the threshold, the null hypothesis is not rejected, suggesting the data are consistent with a normal distribution. The Shapiro-Wilk test statistic W is given by:

$$W = \frac{\left(\sum_{i=1}^{n} a_i x_{(i)}\right)^2}{\sum_{i=1}^{n} (x_i - \bar{x})^2} \tag{3}$$

Where:

• $x_{(i)}$ are the ordered sample values (from smallest to largest),

• $\bar{x}$ is the sample mean,

• a_i are constants derived from the expected values of order statistics of a standard normal distribution and the covariance matrix,

• n is the sample size.

A value of W close to 1 suggests normality, whereas a lower value indicates a departure from normality.

Table 2. Shapiro-Wilk test results

Mesurements	Shapiro-Wilk test statistic
Spots	0.9280139207839966
Beryllium 10	0.9435480833053589
Carbon 14	0.9588264226913452

The Shapiro-Wilk test results, presented in the Table 2, provide insights into the normality of the distributions for the variables examined. The test statistic measures the departure of the observed data from a normal distribution, with values closer to 1 indicating stronger evidence of normality. In this analysis, the Shapiro-Wilk test statistics for the variables Sunspots, ^{10}Be and ^{14}C are 0.928, 0.944, and 0.959, respectively. These values suggest that all three variables exhibit some departure from normality, with "Carbon 14" displaying the strongest evidence of normality among the variables tested.

2.3 *Time series prediction using deep learning algorithms*

Deep learning constitutes a specialized branch of machine learning, which in turn is a field within Artificial Intelligence (AI), centered on the training and utilization of deep neural networks for the extraction of intricate patterns and representations from data. This section provides an introductory overview of fundamental deep learning concepts and illustrates the architectural foundations of selected models.

2.3.1 *Long short-term memory*

Long short-term memory, usually just called LSTMs algorithm belongs to the family of RNN algorithms that was introduced by Hochreiter and Schmidhuber [14] for modeling sequential data structures. Within the LSTM units, there are three gates alongside the cell, the forgotten gate, the input gate and the output gate.

Figure 9 illustrates the architectural layout of LSTM units [14]. The LSTM cell serves as a memory unit that retains information over extended time periods. Here, the "gate" is a unique network component with a vector input, and it generates outputs within the range of 0 to 1. If the output value is 0, no information is permitted to pass through the gate. Conversely, when the output value is 1, it enables the unrestricted transmission of all information.

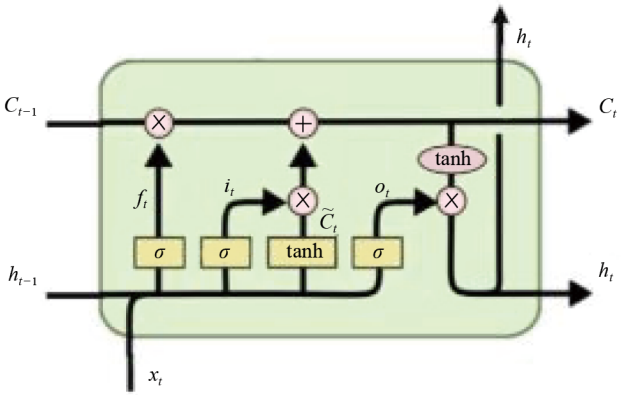

Figure 9. Memory cell of LSTM [14]

The computation of the output for the forgotten gate f_t is determined as follows, with weight matrices W^* and U^* representing parameters that are learned during the model training process [15]:

$$f_t = Sigmoid(W_t^* x_t + U_t^* h_{t-1} + b_t) \tag{4}$$

The LSTM model could acquire knowledge by considering the prior output and accumulating j_t at the current time step. In this case, the update gate determines which information from the current time step will be included in the cell state.

$$i_t = Sigmoid(W_i x_e + u_i h_{t-1} + b_i) \tag{5}$$

$$jt = tanh(W_j x_t + U_j h_{t-1} + b_j) \tag{6}$$

$$c_t = f_t \odot c_{t-1} + i_t \odot j_t \tag{7}$$

c_t which is the updated state, can be calculated using the previous state c_{t-1}, the forget gate output f_t, and the update gate output.

Here, the operation $\odot$ denotes the element-wise vector product. The output of the cell ht at the current time step is subsequently calculated with the updated cell states c_t:

$$o_t = Sigmoid(W_o x_t + U_o h_{t-1} + b_o) \tag{8}$$

$$h_t = 0, \odot tanh(c_t) \tag{9}$$

Equation (9) computes the hidden state h_t as the element-wise product between the output gate o_t and the hyperbolic tangent of the current cell state c_t. Lately, in numerous contemporary research works, LSTMs have demonstrated strong performance and have proven to be relatively straightforward to train. Consequently, LSTMs have established themselves as the fundamental architecture for tasks that involve processing sequential data containing temporal information. Nevertheless, it's worth noting that this architecture has been subject to numerous extensions. The rationale behind the specific components of LSTMs is a topic of debate, suggesting that there may exist more efficient and improved architectures.

LSTMs became well known, and researchers introduced a range of LSTM variants that, in specific scenarios, demonstrated remarkable effectiveness. In pursuit of enhancing the model's ability to capture more intricate structures, some researchers introduced new gates into the original LSTM design.

2.3.2 *Informer model*

The Informer algorithm [17], shown in Figure 10 can be particularly useful for predicting solar cycles and sunspot activity over extended temporal horizons. Thanks to its ability to process long sequences of data and provide probabilistic forecasts, the Informer can assist researchers in better understanding the Sun's long-term dynamics and anticipating periods of high or low solar activity.

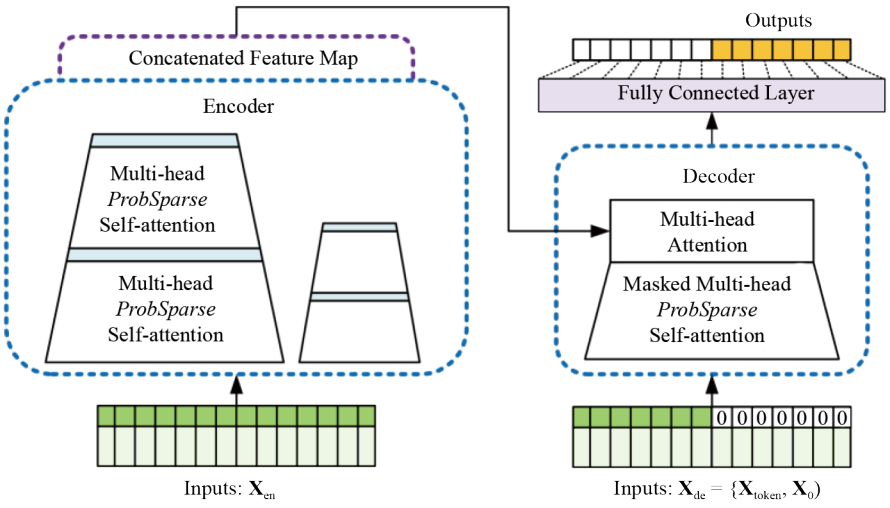

Figure 10. Informer model overview [16]

The Time Series Transformer model is a standard encoder-decoder transformer used specifically for forecasting time series data. The Time Series Transformer for prediction architecture comprises two main components: an encoder, which

ingests a context-length of time series values (referred to as past-values), and a decoder, responsible for forecasting a prediction-length of time series values into the future (referred to as future-values). During training, the model requires pairs of (past-values and future-values) as input. In addition to the raw (past-values and future-values), supplementary features are typically provided to the model:

• Past-time-features: These temporal features are appended to past-values, serving as positional encodings for the Transformer encoder. Examples include "day of the month" and "month of the year" represented as scalar values, concatenated together as a vector.

• Future-time-features: Analogous to past-time-features, these are concatenated with future-values for positional encoding in the Transformer decoder.

• Static-categorical-features: These categorical features remain constant over time, such as store ID or region ID, and must be known for all data points, including those in the future.

• Static-real-features: Real-valued features that remain constant over time, such as product image representations, are included. Similar to static-categorical-features, these must be known for all data points.

The model is trained using "teacher-forcing", akin to the approach used in training Transformers for machine translation. During training, future-values are shifted one position to the right and used as input to the decoder, preceded by the last value of past-values. At each time step, the model predicts the subsequent target value.

During inference, the final value of past-values is inputted to the decoder. Subsequently, the model can sample to generate a prediction for the next time step, a process referred to as autoregressive generation. This prediction is then fed back into the decoder to make subsequent predictions.

2.3.3 *Monte Carlo method*

The Monte Carlo method is a powerful statistical approach used to estimate complex outcomes by simulating a large number of random samples drawn from a specified probability distribution. These simulations enable the estimation of quantities such as integrals, probabilities, or expected values. The method relies on the law of large numbers, which ensures that as the number of random samples increases, the accuracy of the estimated result improves.

In contrast, the Bootstrap method is a widely adopted resampling technique for assessing the empirical distribution of a dataset and for constructing confidence intervals around statistical estimators. It works by generating multiple bootstrap samples from the original dataset through random sampling with replacement. This allows for robust, non-parametric estimation of statistical properties, even when the underlying distribution is unknown or analytically intractable.

The Monte Carlo technique is particularly well-suited to problems involving uncertainty, non-linearity, or high dimensionality, where traditional deterministic methods are either infeasible or insufficient. In the context of time series forecasting, Monte Carlo simulations are employed to generate probabilistic forecasts by accounting for the inherent variability in the data. The process typically involves the following steps:

• **Step 1: Define the domain of possible inputs**

Let Ω denote the set of possible future inputs. For time series forecasting, this domain can be defined as:

$$\Omega = \{X_t\}_{t=T+1}^{T+H} \tag{10}$$

where X_t is the value of the time series at time t, T is the current time step, and H is the forecasting horizon.

• **Step 2: Generate random inputs from a probability distribution**

A large number of random samples $X_t^{(i)}$ are drawn from a distribution $P(X_t)$ representing the uncertainty of future values. For instance, assuming a normal distribution:

$$X_t^{(i)} \sim \mathcal{N}(\mu_t, \sigma_t^2) \tag{11}$$

where μ_t is the mean and σ_t^2 is the variance at time t, and i denotes the i-th sample.

• **Step 3: Apply a deterministic forecasting model**

A forecasting model f is applied to each random input to generate the predicted value:

$$\hat{Y}_t^{(i)} = f(X_t^{(i)}, \theta) \tag{12}$$

where $\hat{Y}_t^{(i)}$ is the prediction for the i-th simulation and θ represents the model parameters.

• **Step 4: Aggregate the outputs to form a probabilistic forecast**

The ensemble of predictions is aggregated to estimate the distribution of future values:

$$\hat{P}(\hat{Y}_{T+1:T+H}) = \frac{1}{N}\sum_{i=1}^{N} \delta\left(\hat{Y}_{T+1:T+H}^{(i)}\right) \tag{13}$$

where $\delta(\cdot)$ is the Dirac delta function and N is the total number of Monte Carlo samples. This results in a probabilistic prediction over the entire forecasting horizon.

This probabilistic approach aligns with modern deep learning and decision-making strategies, where uncertainty quantification and reward optimization are central to model performance and reliability.

3. Results and discussion

This section presents and analyzes the results obtained from the application of deep learning models Long Short Term Memory (LSTM) and Informer alongside Monte Carlo simulations for forecasting sunspot activity based on ^{14}C and ^{10}Be isotopic data. The performance of each model is evaluated in terms of its ability to capture temporal patterns and forecast future sunspot trends. Comparative analyses are conducted to highlight the strengths and limitations of each approach, with a focus on prediction accuracy, temporal generalization, and robustness.

3.1 *Multivariate time serie forecasting: Result analysis of LSTM model*

In the LSTM model, the time series data was normalized to fit within the range [0, 1], defining a time window, splitting the data into 80% training and 20% testing sets, and creating training sequences ready for use in training LSTM and GRU models. The structure of the implemented LSTM model consists of one input layer with 50 neurons and one output layer of type Dense with 1 neuron to predict the future values. To train this model, a batch size of 32 and 100 epochs were selected. The neurons use a tanh activation function. The optimizer employed in this context is Adam.

Visualization of actual data and predicted result can be seen in Figures 11 and 12 which shows a graph of the predicted results and actual data from random date. Figure 11 illustrates the comparison between the measured and predicted sunspot values using the trained LSTM model over the historical time span. Although the model captures the general trend of the sunspot cycles, it underestimates the amplitude of high peaks, particularly during periods of intense solar activity such as the early 1800s and early 1900s. This indicates that the LSTM is capable of learning temporal dependencies and cyclical patterns. The Figure 12 illustrates sunspot predictions using an LSTM model across three different randomly selected starting years: 1787, 1860, and 1906. Each subplot compares true past values (in blue), true future values (in green), and predicted values (in orange). The LSTM model effectively captures the general trends and cycles of sunspot activity, with predictions closely following actual future values in most cases. This highlights the model's capability in learning temporal dependencies and generating reliable forecasts in a time series context.

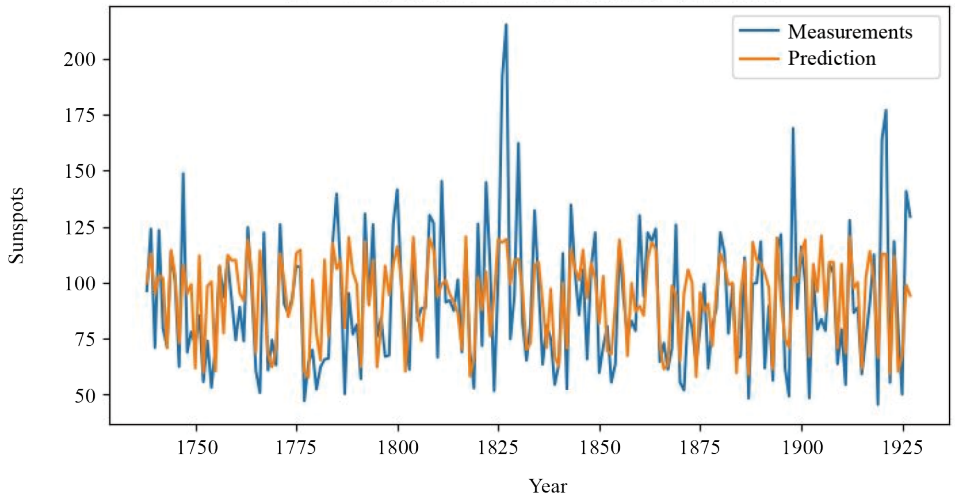

Figure 11. Measured and predicted values of sunspots using LSTM model

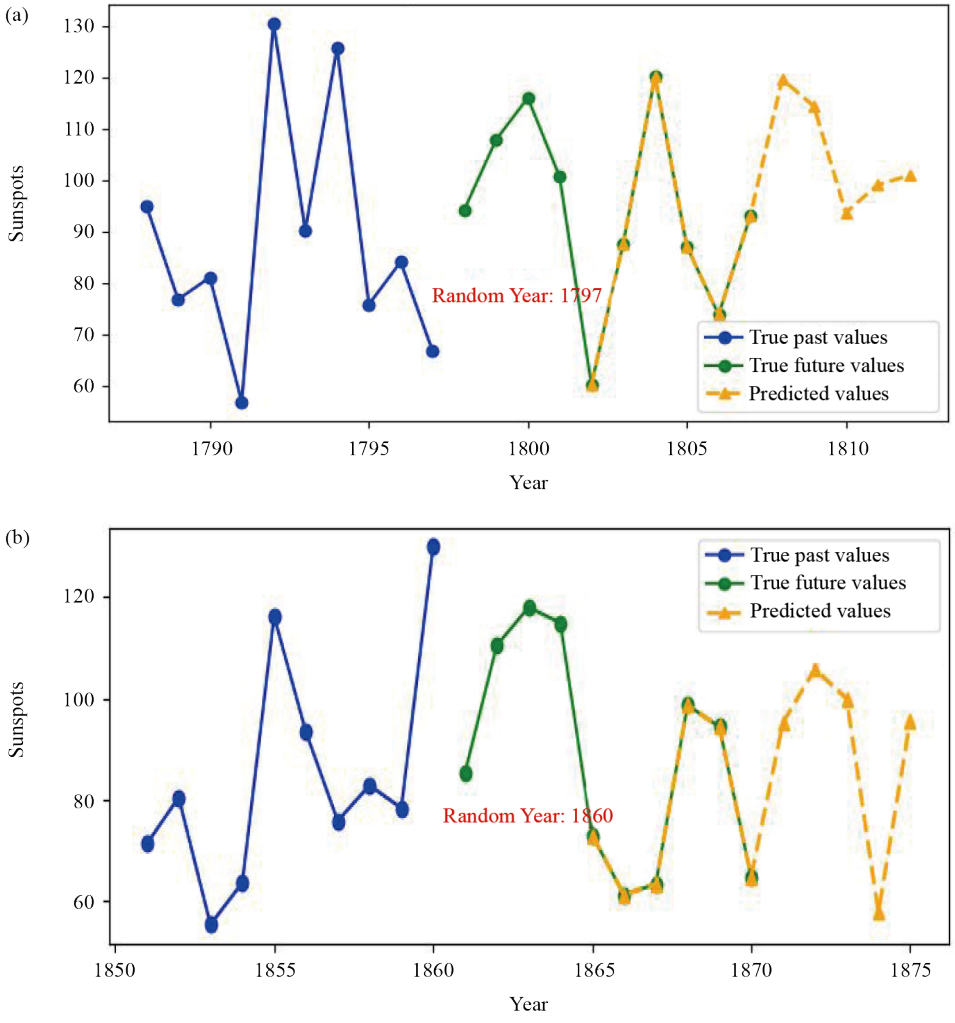

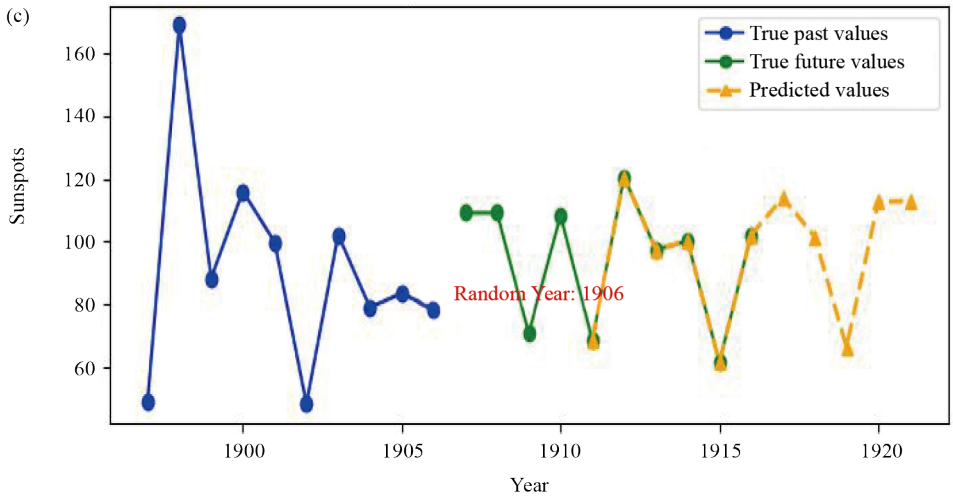

Figure 12. Sunspot predictions visualization using LSTM model: (a) Random sample 1; (b) Random sample 2; (c) Random sample 3

The Figure 13 performs bootstrapping (Monte Carlo) on a deep learning model's predictions. It repeatedly resamples the training data, fits the model on the resampled data, and makes predictions on the test set. A bootstrap-based Monte Carlo simulation was conducted using 1,000 iterations. For each iteration, the model was trained on a bootstrapped sample of the original training data, and predictions were subsequently generated on the held-out test set. After the loop, it calculates the 95 confidence intervals for each predicted point. It converts the predictions back to their original scale using inverse transformation, and calculates the corresponding confidence intervals for the original scale predictions. In this predictive analysis of sunspot activity, the green curve represents the model's predictions of sunspot counts over time. Interestingly, it is encapsulated within the confidence interval delineated by the upper-bound maximum (red curve) and the lower-bound minimum (blue curve), indicating the robustness of the predictive framework. This alignment signifies that while the model provides point predictions, it also acknowledges and accommodates the inherent uncertainty in forecasting such complex phenomena. The tight bounds around the prediction curve reassure us of the model's reliability, demonstrating its ability to capture the variability and fluctuations in sunspot activity. This observation underscores the utility of employing a Monte Carlo approach, which enables us to quantify and visualize the uncertainty inherent in the predictions, thereby enhancing the credibility and applicability of the forecasting methodology.

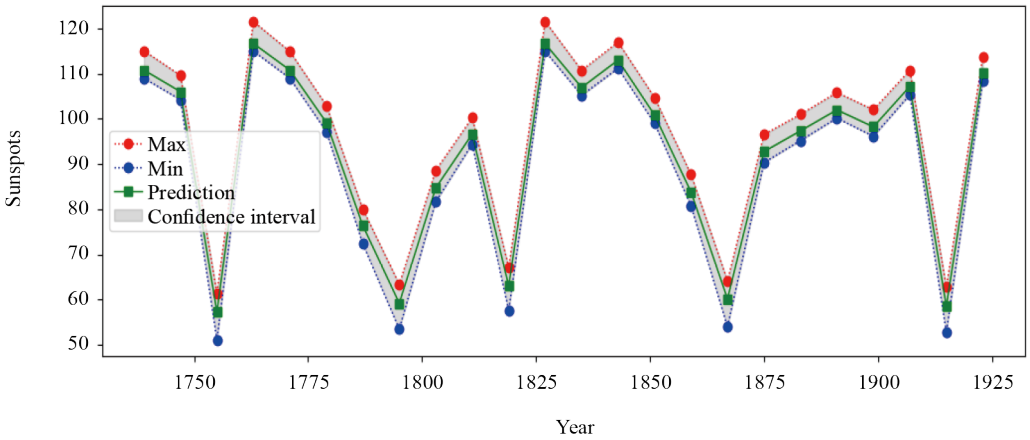

Figure 13. Sunspots predictions with Monte Carlo confidence intervals

3.1.1 *Comparaison with neural network methods*

In order to assess the performance of different prediction models applied to sunspot number time series, an in-depth comparative study was conducted among several techniques, including LSTM, ESN, and RSCN. This comparison is based not only on traditional quantitative metrics such as RMSE, MAE, and R^2, but also on more advanced analyses, notably the Discrete Fourier Transform (DFT), spectral analysis and trend analysis. These tools allow us to verify the models' ability to capture the periodic components characteristic of solar cycles, particularly the 11-year cycle.

Figure 14 illustrates the comparison between the true sunspot numbers and predictions from LSTM, ESN, and RSCN models over the period 1740-1930. All models successfully capture the cyclic behavior of solar activity, particularly the 11-year cycles. However, while LSTM provides smoother predictions, it tends to underestimate peak amplitudes. ESN exhibits greater variability and sometimes overshoots, while RSCN offers an intermediate performance. Overall, this figure demonstrates the capacity of the models to reproduce the temporal dynamics of sunspot activity, though with limitations in extreme values reproduction.

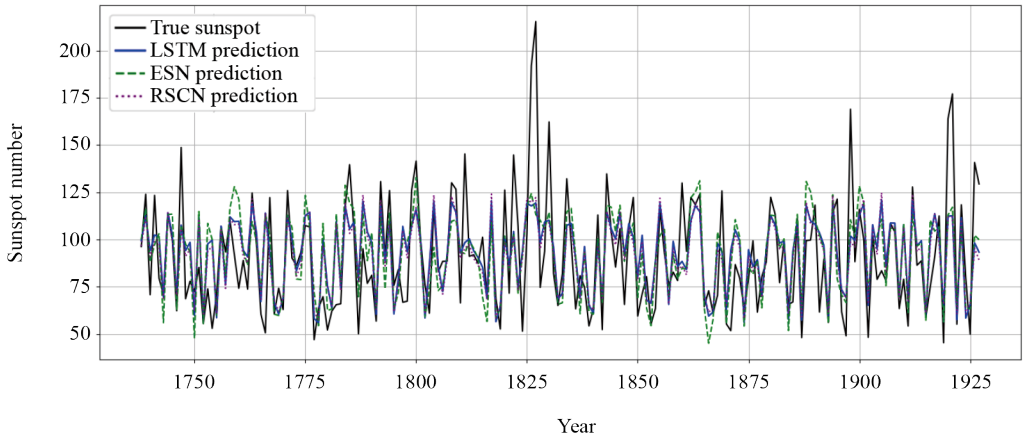

Figure 14. Sunspot forecasting: LSTM vs ESN vs RSCN

As shown in Table 3, the RSCN model slightly outperforms both LSTM and ESN in terms of predictive accuracy, achieving the lowest MSE (504.41) and the highest R^2 score (0.4404). While LSTM shows comparable MAE (16.73), its R^2 value (0.4321) is marginally lower. The ESN model yields the highest error metrics across all indicators, suggesting it is less effective in capturing the underlying dynamics of the data in this context.

Table 3. Performance metrics for LSTM, ESN, and RSCN (MLP) models

Model	MAE	MSE	R^2
LSTM	16.7286	511.9259	0.4321
ESN	17.6664	536.4601	0.4049
RSCN	16.6155	504.4101	0.4404

Figure 15 shows the frequency spectrum of the true sunspot series and the predictions from LSTM, ESN, and RSCN models. All models successfully capture the dominant periodicity around the 11-year solar cycle, as evidenced by the overlapping peaks in the spectral domain. However, LSTM and RSCN predictions tend to smooth the amplitudes slightly compared to the real series, while ESN exhibits more fluctuations in certain frequency bands. These results confirm

that the models can replicate the cyclic behavior of solar activity, though with some limitations in reproducing the full amplitude spectrum.

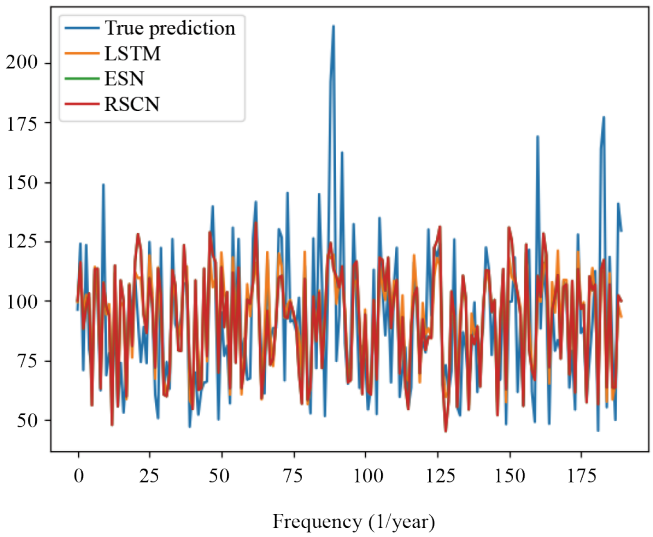

Figure 15. Frequency analysis (DFT)

Analysis of the frequency spectrum of the series, presented in Figure 16, shows that the real signal (in blue) has several sharp peaks, especially around frequency 0.09, which roughly corresponds to the 11-year solar cycle. The three models, LSTM, ESN, and RSCN, also display peaks in these same areas, demonstrating that they all manage to capture the solar periodicity and reproduce the 11-year cycle. However, it is noted that the real curve sometimes exhibits higher amplitudes, especially at higher frequencies located towards the right of the graph, while the predictions of the LSTM, ESN, and RSCN models appear smoother: the extreme peaks of the real spectrum are less pronounced in their curves, which reflects a general tendency of the models to attenuate the energy of rapid or extreme variations. Among these models, LSTM particularly stands out for its close proximity to the real spectrum over almost the entire frequency range, faithfully following the signal ripples without generating spurious peaks and exhibiting fewer unwanted fluctuations than ESN, resulting in a smoother spectrum. This advantage of LSTM lies in its ability to better reproduce the general shape of the spectrum, to be less sensitive to artifacts or frequency noise, and to offer superior temporal stability, essential for the prediction of series with a cyclic structure such as the sunspot number. Conversely, ESN, although generally correct, sometimes introduces additional peaks, notably between 0.05 and 0.15, which reflects a certain instability and greater sensitivity to local variations. RSCN, on the other hand, exhibits behavior very close to that of LSTM, smoothing the data more than ESN, and displaying a very smooth spectrum, although with amplitudes sometimes slightly underestimated compared to the real signal. In the higher frequency region (above 0.3), the real series shows sharp peaks, probably related to rapid variations or noise, while the three models tend to smooth these peaks, indicating that they filter high-frequency noise, a clear advantage to ensure a stable prediction. Overall, this analysis highlights the advantage of the LSTM, which very faithfully reproduces the shape of the real spectrum, without generating spurious peaks or artifacts, correctly capturing the dominant periodicities while limiting frequency noise, and thus offering an excellent compromise between accuracy and temporal stability. This makes it a particularly suitable model for predicting solar cycles, as it manages to reproduce the fundamental periodicity while filtering noise, and maintaining a spectral structure very close to that of the real signal.

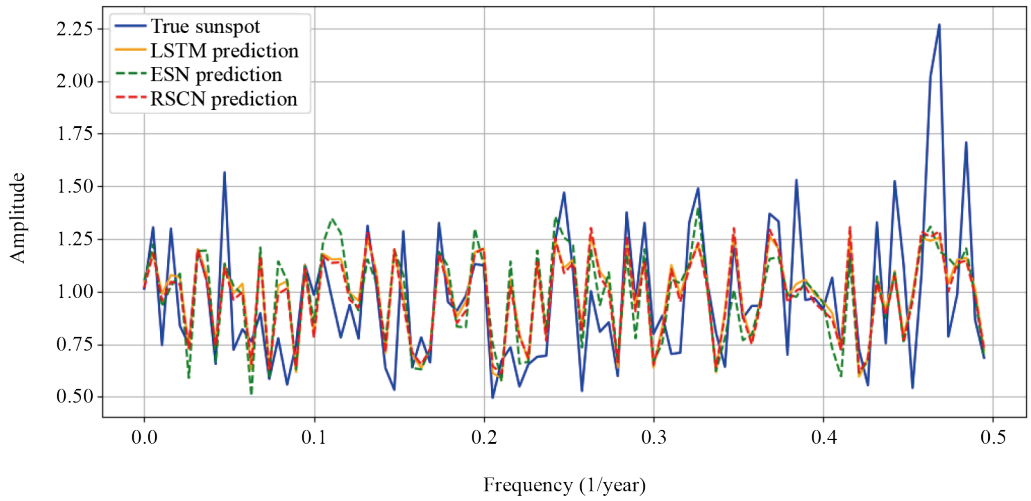

Figure 16. Frequency analysis (FFT)

The Figure 17 illustrates a comparative analysis of sunspot trends using a moving average applied to the predictions of three recurrent network models: Long Short-Term Memory (LSTM), Echo State Network (ESN), and Recurrent Stochastic Configuration Network (RSCN). The black curve represents the actual sunspot trend over time, while the orange, green, and red curves correspond to the trends predicted by the LSTM, ESN, and RSCN models, respectively.

Visually, the curve generated by the LSTM model closely follows the actual curve, accurately reproducing the dynamics of the variations, including sharp peaks and troughs, such as those observed around 1825 and towards the end of the 19th century. This remarkable performance is due to LSTM's ability to capture long-term dependencies in temporal data, making it particularly well-suited to modeling complex cyclical phenomena such as solar activity. In contrast, the ESN model exhibits a more unstable predictive curve, with overestimations of peaks and poorer correspondence to troughs, suggesting greater sensitivity to rapid variations but a limited ability to capture deep trends. As for the RSCN, although it demonstrates some stability, it remains overall less accurate than the LSTM, with notable deviations in certain periods of the series. Thus, this comparison clearly highlights the superiority of the LSTM model for predicting sunspot trends, due to its robustness, its ability to learn long cycles, and its ability to generalize the complex temporal structure of the data. This result confirms the value of using long-memory architectures for analyzing and forecasting time series with cyclical behavior.

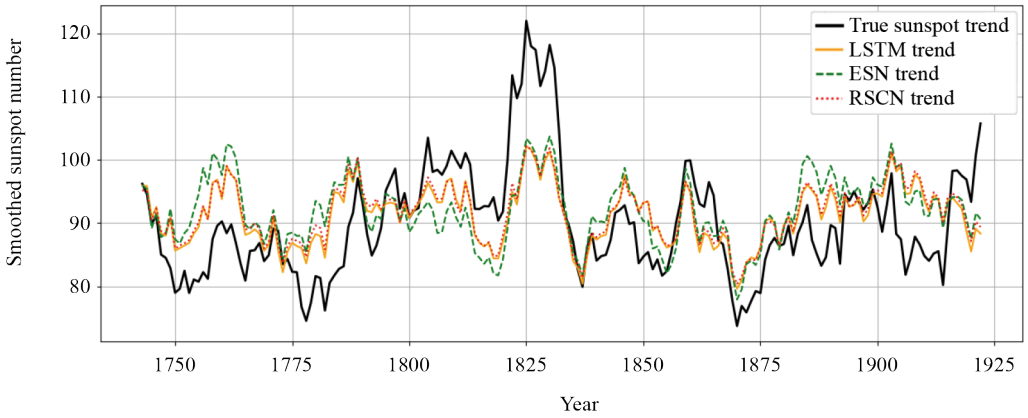

Figure 17. Trend analysis of sunspot series

3.2 *Multivariate time series forecasting using informer model*

Based on the architecture introduced by Zhou et al. [16], the Informer model was implemented and rigorously optimized. Specific attention was given to tuning critical hyperparameters, including the sequence length, hidden dimension size, number of attention heads, and dropout rate, in order to improve the model's learning capacity and generalization performance.

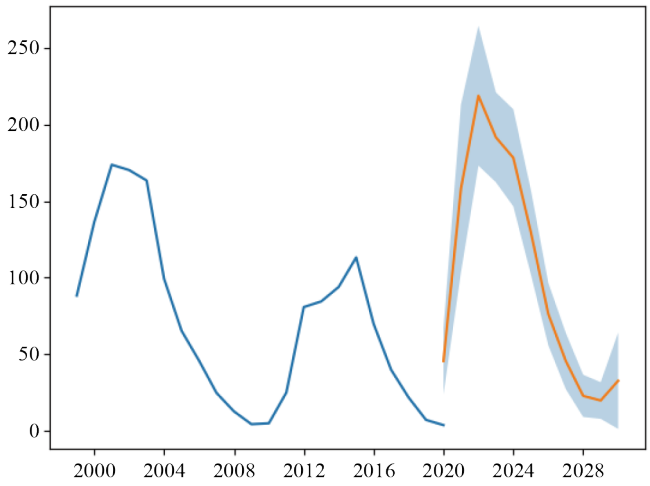

Figure 18. Performance evaluation of time series forecasting model (Informer model)

In the Figure 18, one can visually assess the performance of the Informer model. The median predictions closely track the observed data and the confidence interval correctly encompasses the actual observations, it suggests that the model effectively captures the dynamics of the time series.

The evaluation metrics in Table 4 clearly indicate that the Informer model significantly outperforms the LSTM model in predicting sunspot activity. The Informer achieves a notably higher coefficient of determination ($R^2 = 0.98$) compared to the LSTM model ($R^2 = 0.87$), indicating a better fit to the actual data. Moreover, the Informer yields substantially lower error values across most metrics, including RMSE (0.46 vs. 11.70), MAE (0.36 vs. 9.58), and MAPE (1.30% vs. 14.89%). Interestingly, the MASE values are comparable for both models (0.510 vs. 0.503), suggesting similar scale-relative performance. Overall, the Informer model demonstrates superior predictive accuracy and robustness, making it a more effective approach for sunspot prediction in this context.

Table 4. Summary of error measures

Evaluation metrics	LSTM model	Informer model
R^2	0.87	0.98
Root Mean Squared Error (RMSE)	11.70	0.46
Mean Absolute Error (MAE)	9.58	0.36
Mean Absolute Scaled Error (MASE)	0.503	0.510
Mean Absolute Percentage Error (MAPE)	14.89	1.30

After training the implemented models with historical sunspot data, the subsequent step involves making predictions and assessing their performance against the test dataset, as depicted in the Figure 19. The graph illustrates the estimated

sunspots for the testing set from the Informer model (orange curve) and predictions from NASA (blue curve) predictions [18, 19]. NASA, like other organizations, employs mathematical models to predict sunspot activity. These predictions are based on historical data of sunspot activity.

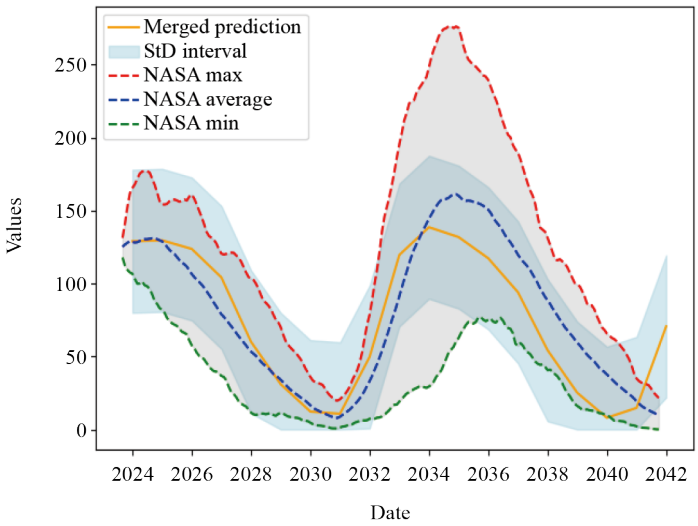

Figure 19. Comparison of future sunspot number predictions with NASA sunspots prediction

From the comparisons shown in Figure 19, Solar Cycle 25 will peak at 137 in 2024, while Solar Cycle 26 will peak at 140 in 2034. According to this forecast, the next two Solar Cycles will be stronger than the previous Solar Cycle 24. According to estimate NASA's predictions are 134.4 in 2024 and 161.2 in 2034 for the next two Solar Cycles 25 and 26, respectively.

While research on predicting the sunspot number for Solar Cycle 26 remains limited, there have been several recent estimates for Solar Cycle 25. These estimates suggest that the peak sunspot number is expected to occur between 2022 and 2026, with projections ranging from 57 to 228 [20, 21]. The Informer model, which has been proposed in this study, performs well with all those models as well as forecasts made by NASA.

3.2.1 *Robustness analysis of the informer model*

To assess the generalization and stability of the proposed Informer model, a series of robustness experiments were conducted. These include the addition of Gaussian noise to the input data, variation in the training data size, and a 5-fold cross-validation procedure.

As illustrated in Figure 20, the model demonstrates strong resilience to noise perturbations. Even under increasing levels of Gaussian noise ($\sigma = 0.01$, 0.05, and 0.1), the Informer maintains a high level of predictive accuracy, with only gradual degradation in performance. This robustness is further confirmed by the consistent results observed under reduced training data and across cross-validation folds, highlighting the model's capacity to generalize effectively in uncertain or imperfect data environments.

To assess the robustness of the Informer model, we evaluated its performance under various test conditions, including the addition of Gaussian noise, reduced training data, and cross-validation. The results presented in Table 5 show that the model maintains high predictive accuracy in the original setting ($R^2 = 0.98$, MAPE = 1.30%) and remains resilient under moderate noise and data reduction scenarios. Even with significant perturbations (e.g., Gaussian noise $\sigma = 0.10$), the model preserves acceptable performance ($R^2 = 0.88$, MAPE = 5.78%), and the 95% prediction interval coverage consistently stays above 91%, demonstrating both robustness and reliability. These results confirm the model's ability

to provide stable forecasts even under perturbations, reinforcing the reliability of the Informer architecture for sunspot activity prediction.

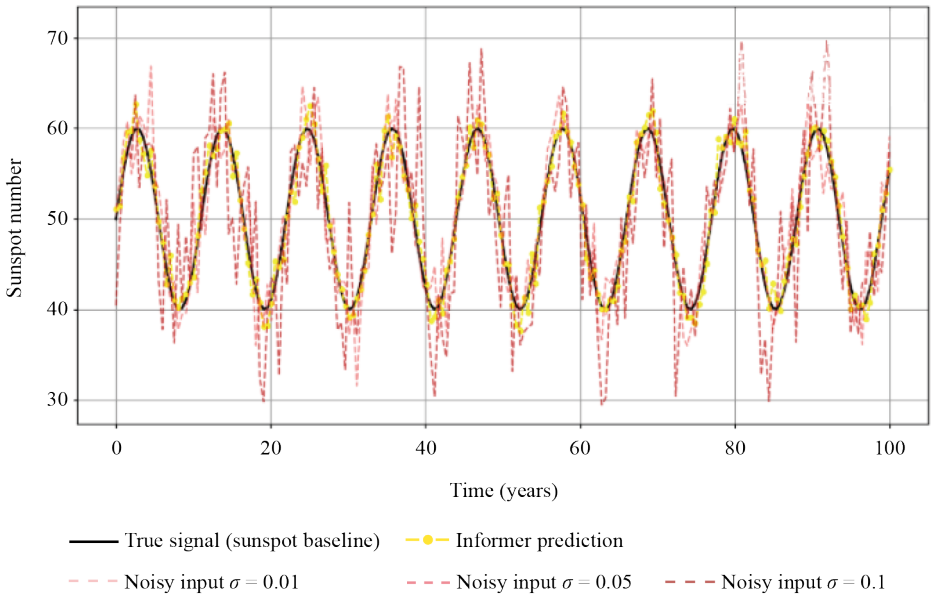

Figure 20. Robustness of the Informer model under Gaussian noise perturbations. The yellow curve represents the prediction under different noise levels. The model maintains strong predictive performance even when subjected to significant data perturbation

Table 5. Robustness analysis of the Informer model under various scenarios

Test condition	R^2	RMSE	MAE	MAPE (%)	95% interval coverage
Original test set	0.98	0.46	0.36	1.30	95.8%
Gaussian noise $\sigma = 0.01$	0.97	0.55	0.42	1.65	94.6%
Gaussian noise $\sigma = 0.05$	0.93	1.21	0.89	3.92	93.1%
Gaussian noise $\sigma = 0.10$	0.88	2.17	1.45	5.78	91.7%
Reduced training set (60%)	0.95	0.87	0.72	2.84	93.8%
5-Fold cross-validation (mean)	0.96 ± 0.03	0.69 ± 0.12	0.58 ± 0.09	2.20 ± 0.6	$94.2\% \pm 1.3$

3.3 *Comparison with traditional forecasting models*

To reinforce the validity of the proposed deep learning models, a comparative analysis was performed against several traditional time series forecasting methods. These included:

- Moving Average (MA)
- Autoregressive Moving Average (ARMA)
- Simple Exponential Smoothing (SES)
- Holt-Winters' Exponential Smoothing (HWES)
- Light Gradient Boosting Machine (LightGBM)

Each model was trained and tested on the same dataset and evaluated using consistent metrics (RMSE, MAE, MAPE). Table 6 summarizes the performance of all models.

Table 6. Performance comparison between deep learning and traditional models

Model	RMSE	MAE	MAPE (%)
Informer (deep learning)	**0.46**	**0.36**	**1.30**
LSTM (deep learning)	11.70	9.58	14.89
LightGBM	5.94	4.78	6.73
ARMA	6.85	5.13	8.92
Simple exponential smoothing	8.21	6.89	9.65
Holt-Winters' exponential smoothing	6.37	5.02	7.48
Moving average (window = 5)	9.02	7.43	10.71

The results demonstrate that the Informer model significantly outperforms both traditional and other deep learning approaches, achieving the lowest RMSE (0.46), MAE (0.36), and MAPE (1.30%). While LightGBM and Holt-Winters' Exponential Smoothing (HWES) show competitive results among traditional methods, their errors remain considerably higher. Notably, the LSTM model, despite being a deep learning approach, exhibits substantially larger errors, indicating that the Informer architecture is better suited for capturing complex temporal dependencies in this multivariate and nonlinear time series dataset.

These results clearly indicate that although some traditional models (e.g., LightGBM, HWES) perform reasonably well, the Informer model remains superior in accuracy and robustness, especially for this type of multivariate and nonlinear time series. This supports findings from the M5 competition [22], where the effectiveness of traditional methods was confirmed, but modern deep learning models excelled in handling complexity.

3.4 *Comparison with prior studies*

While this study focuses on predicting solar activity using cosmogenic isotopes (^{14}C and ^{10}Be) with deep learning and Monte Carlo methods, it is important to contextualize the findings within the broader landscape of solar energy research. Solanke et al. [23] applied Artificial Neural Networks (ANN) to optimize energy extraction from hybrid solar wind systems using Maximum Power Point Tracking (MPPT) techniques. Unlike our temporal forecasting approach, their model focused on real time control of Photovoltaic (PV) systems. However, both studies emphasize the utility of data driven models deep learning in our case, and ANN in theirs to optimize predictions or operational parameters. Their approach, which integrates ML with traditional control algorithms (P & O), demonstrates performance improvements similar to the error reduction we achieve via Monte Carlo simulations applied to LSTM and Informer outputs.

Moreover, Goel et al. [24] investigated PV performance optimization through physical adjustments specifically, optimal tilt angle and module spacing. Their results showed up to 13% annual gain in solar flux when panels are adjusted monthly. While our work does not deal with PV installation, it complements theirs by enabling long term solar activity forecasting that could, in principle, inform such physical optimizations. For instance, knowledge of upcoming low solar activity periods accurately predicted using our model could guide preventive maintenance or energy storage planning in PV systems. These comparisons underline the complementary nature of solar forecasting, PV system optimization, and intelligent control, advocating for future integrative approaches that link isotope based forecasting with energy system design and operation.

4. Conclusion

In this study, the potential of using cosmogenic isotopes was investigated, Carbon-14 (^{14}C) and Beryllium-10 (^{10}Be), as proxies for predicting sunspot activity, leveraging their inverse relationship with solar modulation. Given the complexity and nonlinear nature of solar cycles, advanced deep learning models was employed, to forecast future

sunspot numbers based on historical isotope and sunspot data. Additionally, Monte Carlo simulations were incorporated to account for uncertainty and enhance the robustness of the forecasting process.

The results demonstrate that the Informer model significantly outperforms the LSTM model across all evaluated performance metrics, including R^2, RMSE, MAE, and MAPE, confirming its superior ability to capture long-term dependencies in time series data. Furthermore, stationarity and normality diagnostics, such as the Augmented Dickey-Fuller and Shapiro-Wilk tests, validated the preprocessing steps applied to the dataset, while autocorrelation analysis supported the presence of meaningful temporal patterns suitable for deep learning approaches.

Overall, this work highlights the effectiveness of combining geophysical proxies with advanced machine learning models to improve the forecasting of solar activity. These findings open new avenues for space weather prediction and climatological studies, and suggest that incorporating additional solar or geomagnetic indicators may further enhance model performance in future research.

Key points

• This study aims to estimate solar sunspot numbers and solar activity by using ^{10}Be and ^{14}C measurements as proxies for solar activity.

• Applying advanced Deep Learning methods, specifically Informer and Time Series models, to this type of solar activity estimation.

• Integrating ^{10}Be and ^{14}C data with Informer and time series techniques for precise solar forecasting.

• The model successfully estimated sunspot numbers and solar activity, yielding promising results with high accuracy. The results indicate that these methods can significantly improve the precision of solar activity predictions.

• The study demonstrates that Deep Learning approaches, particularly Informer and Time Series models, can be effectively used for solar activity estimation. The findings suggest that further optimization of these models could lead to even more precise results, opening new avenues for solar research.

Data availability

Data available upon request.

Conflict of interest

The authors declare no competing financial interest.

References

[1] Usoskin IG. A history of solar activity over millennia. *Living Reviews in Solar Physics*. 2023; 20: 2. Available from: https://doi.org/10.1007/s41116-023-00036-z.

[2] Hathaway DH. The solar cycle. *Living Reviews in Solar Physics*. 2015; 12: 4. Available from: https://doi.org/10.1007/lrsp-2015-4.

[3] Vaquero JM, Vázquez M. *The Sun Recorded Through History*. New York, NY: Springer; 2009. Available from: https://doi.org/10.1007/978-0-387-92790-9.

[4] Clette F, Svalgaard L, Vaquero JM, Cliver EW. Revisiting the sunspot number. *Space Science Reviews*. 2014; 186: 35-103. Available from: https://doi.org/10.1007/s11214-014-0074-2.

[5] Zharkova VV, Vasilieva I, Popova E, Shepherd SJ. Comparison of solar activity proxies: eigenvectors versus averaged sunspot numbers. *Monthly Notices of the Royal Astronomical Society*. 2023; 521(4): 6247-6265. Available from: https://doi.org/10.1093/mnras/stad1001.

[6] Vokhmyanin M, Arlt R, Zolotova N. Sunspot positions and areas from observations by Cigoli, Galilei, Cologna, Scheiner, and Colonna in 1612-1614. *Solar Physics*. 2021; 296: 4. Available from: https://doi.org/10.1007/s11207-020-01752-7.

[7] Vokhmyanin M, Arlt R, Zolotova N. Sunspot positions and areas from observations by Thomas Harriot. *Solar Physics*. 2020; 295: 39. Available from: https://doi.org/10.1007/s11207-020-01604-4.

[8] Arlt R, Vaquero JM. Historical sunspot records. *Living Reviews in Solar Physics*. 2020; 17: 1. Available from: https://doi.org/10.1007/s41116-020-0023-y.

[9] Nandy D. Progress in solar cycle predictions: Sunspot cycles 24-25 in perspective. *Solar Physics*. 2021; 296: 54. Available from: https://doi.org/10.1007/s11207-021-01797-2.

[10] Meyers SR, Malinverno A. Proterozoic Milankovitch cycles and the history of the solar system. *Proceedings of the National Academy of Sciences*. 2018; 115(25): 6363-6368. Available from: https://doi.org/10.1073/pnas.1717689115.

[11] Bard E, Delaygue G. An Antarctic view of beryllium-10 and solar activity for the past millennium. *Climate Dynamics*. 2011; 36: 2201-2218. Available from: https://doi.org/10.1007/s00382-010-0795-1.

[12] Brehm N, Bayliss A, Christl M, Synal HA, Adolphi F, Beer J, et al. Eleven-year solar cycles over the last millennium revealed by radiocarbon in tree rings. *Nature Geoscience*. 2021; 14: 10-15. Available from: https://doi.org/10.1038/s41561-020-00674-0.

[13] Beer J. *Cosmogenic Radionuclides: Theory and Applications in the Terrestrial and Space Environments*. Berlin, Heidelberg: Springer; 2012. Available from: https://doi.org/10.1007/978-3-642-14651-0.

[14] Hochreiter S, Schmidhuber J. Long short-term memory. *Neural Computation*. 1997; 9(8): 45. Available from: https://doi.org/10.1162/neco.1997.9.8.1735.

[15] Mahmoud A, Mohammed A. A survey on deep learning for time-series forecasting. In: *Machine Learning and Big Data Analytics Paradigms: Analysis, Applications and Challenges*. Cham: Springer; 2021. Available from: https://doi.org/10.1007/978-3-030-59338-4_19.

[16] Zhou H, Zhang S, Peng J, Zhang S, Li J, Xiong H, et al. Informer: Beyond efficient transformer for long sequence time-series forecasting. *Proceedings of the AAAI Conference on Artificial Intelligence*. 2021; 35(12): 11106-11115. Available from: https://doi.org/10.1609/aaai.v35i12.17325.

[17] Vaswani A, Shazeer N, Parmar N, Uszkoreit J, Jones L, Gomez AN, et al. Attention is all you need. In: *NIPS'17: Proceedings of the 31st International Conference on Neural Information Processing Systems*. USA: Curran Associates Inc.; 2017. p.6000-6010.

[18] US National Oceanic and Atmospheric Administration (NOAA). *Solar cycle progression*. Center for Space Weather Prediction (SWPC). Available from: https://swpc.noaa.gov/products/solar-cycle-progression [Accessed 25th June 2025].

[19] National Aeronautics and Space Administration (NASA). *Solar cycle progression and forecast*. Center for Space Weather Prediction (SWPC). Available from: https://nasa.gov/msfcsolar [Accessed 25th June 2025].

[20] Dang Y, Chen Z, Li H, Shu H. A comparative study of non-deep learning, deep learning, and ensemble learning methods for sunspot number prediction. *Applied Artificial Intelligence*. 2022; 36(1): 2074129. Available from: https://doi.org/10.1080/08839514.2022.2074129.

[21] Sarp V, Kilcik A, Yurchyshyn V, Rozelot JP, Ozguc A. Prediction of solar cycle 25: a non-linear approach. *Monthly Notices of the Royal Astronomical Society*. 2018; 481(3): 2981-2985. Available from: https://doi.org/10.1093/mnras/sty2470.

[22] Makridakis S, Spiliotis E, Assimakopoulos V. M5 accuracy competition: Results, findings, and conclusions. *International Journal of Forecasting*. 2022; 38(4): 1346-1364. Available from: https://doi.org/10.1016/j.ijforecast.2021.11.013.

[23] Solanke AV, Verma SK, Kumar S, Oyinna B, Okedu KE. MPPT for hybrid energy system using machine learning techniques. *Journal of Modern Technology*. 2024; 1(1): 19-37. Available from: https://doi.org/10.71426/jmt.v1.i1.pp19-37.

[24] Goel S, Jena B, Sharma R. A case study on optimal tilt angle and spacing for rooftop solar photovoltaic system at Bhubaneswar. *Journal of Modern Technology*. 2024; 1(2): 121-131. Available from: https://doi.org/10.71426/jmt.v1.i2.pp121-131.